





Article

Potential Nano/Microcenters of Crystal Nucleation in Reagent-Grade Purity Solvents and Their Differentiation by Fluorescent-Tagged Antiscalant

Konstantin Popov ¹, Yuri Vainer ², Gleb Silaev ^{2,3}, Vladimir Kuryakov ⁴, Maria Trukhina ¹, Elena Koltinova ¹, Vasilii Trokhin ¹, Maxim Oshchepkov ⁵, Maria Butakova ¹ and Alexander Oshchepkov ^{6,7,*}

¹ Applied Technologies Laboratory, JSC "Fine Chemicals R&D Centre", Krasnobogatyrskaya Str. 42, b1, 107258 Moscow, Russia; ki-popov49@yandex.ru (K.P.); truhenyi-mv@yandex.ru (M.T.); alenka2255460@mail.ru (E.K.); vas2184@yandex.ru (V.T.); masha-2134@mail.ru (M.B.)

² Institute of Spectroscopy of the Russian Academy of Sciences, Fizicheskaya Str. 5, 108840 Troitsk, Russia; vainer@isan.troitsk.ru (Y.V.); silaevgleb@mail.ru (G.S.)

³ Faculty of Physics, Higher School of Economics, National Research University, Myasnitskaya Str. 4, 101000 Moscow, Russia

⁴ Oil and Gas Research Institute of RAS, Gubkina Str. 3, 119333 Moscow, Russia; vladimirkuryakov@gmail.com

⁵ Department of Chemical and Pharmaceutical Technologies and Biomedical Pharmaceuticals, Mendeleev University of Chemical Technology of Russia, Miusskaya Sq. 9, 125047 Moscow, Russia; maxim.os@mail.ru

⁶ Organic Chemistry Department, Institute of Chemistry, Martin-Luther-University Halle-Wittenberg, Kurt-Mothes-Straße 2, 06120 Halle, Germany

⁷ Department of Physics, Max Planck Institute for the Science of Light, Staudtstrasse 2, 91058 Erlangen, Germany

* Correspondence: aleksandr.oshchepkov@chemie.uni-halle.de or aleksandr.oshchepkov@mpl.mpg.de

Abstract: A common issue in studies on liquid-phase chemical processes is that the natural solid nanoimpurities present in reagent-grade chemicals are ignored. Little is known about these impurities' nature, sizes, concentrations, and behavior, yet they significantly affect the efficiency of antiscalants in municipal and laboratory solutions. Recent research has focused on: (i) estimating nanoimpurity concentrations in in-house deionized water and semiconductor-grade isopropanol using "light sheet" optical ultramicroscopy, and (ii) visualizing antiscalant sorption on these impurities. Using a fluorescent-tagged antiscalant aminobis(methylenephosphonic acid) (ADMP-F), we tracked its affinity to particulate matter in deionized water and reagent-grade KCl solutions. Our study showed that the total concentration of nanoparticles with a size larger than 20 nm is about 10⁶ units/mL in deionized water and 10⁵ units/mL in isopropanol. Extrapolation of these values to a size ≥ 1 nm resulted in concentrations of 10¹¹ and 10⁸ units/mL. The addition of KCl or ADMP-F significantly increased foreign nanoparticle populations. ADMP-F is selectively adsorbed by only some impurities, while most antiscalant molecules remain as true solution. To our knowledge, this is the first instance of fluorescently labeled aminoalkylphosphonates being able to differentiate particulate matter traces in reagent-grade purity solutions. Therefore, the role of nanoparticles as crystallization centers should be seriously reconsidered, especially in their important application in scale inhibition.

Keywords: fluorescent antiscalants; aminophosphonic acid; deionized water; isopropanol; nano/micro impurities; ultramicroscopy; nanoparticle concentration



Citation: Popov, K.; Vainer, Y.; Silaev, G.; Kuryakov, V.; Trukhina, M.; Koltinova, E.; Trokhin, V.; Oshchepkov, M.; Butakova, M.; Oshchepkov, A. Potential Nano/Microcenters of Crystal Nucleation in Reagent-Grade Purity Solvents and Their Differentiation by Fluorescent-Tagged Antiscalant. *Crystals* **2024**, *14*, 650. <https://doi.org/10.3390/cryst14070650>

Academic Editor: Elizabeth A. Hillard

Received: 1 June 2024

Revised: 6 July 2024

Accepted: 9 July 2024

Published: 15 July 2024



Copyright: © 2024 by the authors. Licensee MDPI, Basel, Switzerland. This article is an open access article distributed under the terms and conditions of the Creative Commons Attribution (CC BY) license (<https://creativecommons.org/licenses/by/4.0/>).

1. Introduction

The spread and impact of hazardous engineered nanoparticles on humans and the environment is a global concern [1–3]. Huge efforts have been made recently towards the elaboration of various safety measures, assessment of the risks associated with the production and circulation of engineered nanomaterials, and the detection and quantification of nanoparticles in the environment [4–6]. At the same time, little is known about the

nature, sizes, and concentrations of natural solid impurities, inevitably present both in the reagent-grade purity liquid chemicals used everyday in laboratories and industrial aquatic systems, e.g., desalination plants, cooling water facilities, municipal tap waters, etc. [7–9].

Solid particle impurities sized ≥ 100 nm are commonly detected at concentrations ranging from 300,000 to 400,000 units per mL in the urban waters of various cities in the EU, USA, and Russia. In our previous study [9], we demonstrated the presence of microparticles sized ≥ 100 nm in purified waters of different purification levels: in-house deionized water (320 units/mL), in Sigma-Aldrich water for chromatography (3000 units/mL), in electronic-grade nitric acid from Avantor Performance Materials (4700 units/mL), and in some other laboratory samples. However, the concentration of nanoimpurities (≤ 100 nm in size), unfortunately, was not assessed due to the lack of an adequate measurement technique.

Meanwhile, it has been demonstrated that such impurities have a serious impact on water electrolysis [10], nucleation efficiency in crystallization processes [11–14], and the results of scale inhibition tests [15,16]. Moreover, the hypothesis has recently been put forward that some organic reactions, run both in aqueous and nonaqueous mediums, are catalyzed exactly by small quantities of “solvophobic admixtures” that provide the specific structuring of reactants on their surface [17,18]. Thus, the problem of natural nanoimpurity quantification, formulated in the present study, may form the basis, not only for scale inhibition and crystallization processes, but also for a much broader spectrum of chemical applications.

As far as no truly pure chemicals exist, solid nanoimpurities are present in most research-grade compounds of p.a. purity, even after special in-lab purification procedures [19]. Thus, the estimation of the concentration of solid nanoparticles in pure liquids becomes a highly relevant task. However, the most sensitive modern tools of quantitative measurement of nanoparticle (NP) concentration, developed for electronic-grade water, are only applicable to fractions larger than 50 nm [20]. Some manufacturers report the possibility of measuring the concentration of particles that are over 20 nm [21] and even over 10 nm [22–24]. However, the most active and abandoned solid impurities correspond to the fraction ranging from 1 to 10 nm [9,14].

Therefore, this present study focuses on forward scattering-based particle counting methods for measuring the total concentration of particulate matter, including the fraction below 20 nm, in in-house deionized water of everyday laboratory use and in extra pure isopropanol. The idea is to use several particle counters with different thresholds to determine the particle concentration and then extrapolate the resulting dependence of the total particle content from the size range of >20 , >30 , >100 , >200 , >300 , and >500 nm to a size of >1 nm.

In addition, the fluorescence-labeled antiscalant (2-(6-morpholino-1,3-dioxo-1H-benzo[de]isoquinolin-2(3H)yl)ethylazanediy)bis(methylenephosphonic acid) (ADMP-F) [25], which is an analog of the commercial antiscalant aminotris(methylenephosphonic acid) (ATMP), was used to study the interaction with solid nanoparticles (Figure 1).

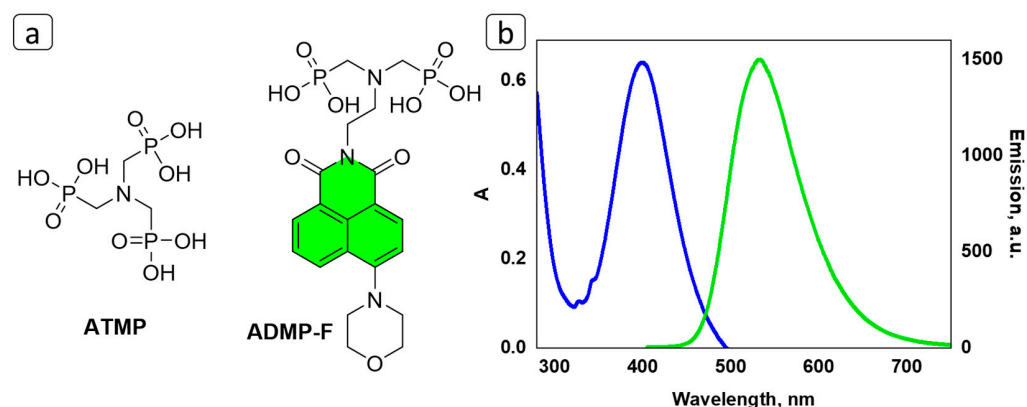


Figure 1. Chemical structure of ATMP and ADMP-F (a); the absorption A (blue line) and emission (green line) spectra of 0.01 mM ADMP-F in water (b) for $\lambda_{\text{ex}} = 400$ nm, slit 2/2. The fluorescent ADMP-F fragment is indicated with green color.

2. Materials and Methods

2.1. Materials

All experiments were run in certified laboratory rooms (ISO 14644-1, class 8) with a limited dust microparticle air phase content, controlled by an air particle counter, Particle Measuring Systems Inc., Boulder, CO, USA with analytical channels 0.3, 0.5, and 5.0 μm . In addition to the usual procedure of washing with acid and base solutions, all glassware (flasks, pipettes, beakers, etc.), as well as ultramicroscopy cuvettes, were rinsed at least three times with deionized water with controlled low nano- and microparticle content before use.

An electronic grade purity isopropanol 13-5 (IP) was used as-purchased from EKOS-1 Co., Moscow, Russia. It was kept in a special double-capped plastic bottle before use. It was then poured directly into quartz cuvettes for ultramicroscopy or into an SLS particle counter cell. Both quartz cuvettes and the cells were triply pre-washed using the same isopropanol portions. No pipettes were used in order to prevent additional contamination by nanoparticles emitted from the pipette walls. The IP sample was analyzed using the ISP-MS technique (iCAP 6300 Duo, Thermo Fisher Scientific, Waltham, MA, USA) for 25 elements, 8 of which are presented in Table 1, while the rest had maintenance on the level of $10^{-7}\%$. The total solid residue was 0.0002%, and basic substance content constituted 99.83%. Thus, IP fits well with the quality of ultra-pure reagents.

Table 1. Isopropanol and deionized water samples characterization by ICP-MS.

Element	Deionized Water *, ppm	Isopropanol *, ppm
Al	0.0000	0.0001
Ca	0.0335	0.0009
Fe	0.0004	0.0002
Mg	0.0031	0.0000
Mn	0.0001	0.0001
P	0.0008	0.0000
S	0.0009	0.0054
Si	0.0320	0.0009

* Concentrations of As, B, Ba, Cd, Co, Cr, Cu, Ni, K, Na, Pb, Sr, Zn, and Sb are less than 0.0002 ppm in water and less than 0.0001 ppm in isopropanol.

The in-house deionized water (Laboratory Reagent Water Type I, ASTM D1193-06(2011), 0.056 $\mu\text{S}/\text{cm}$; pH 5.75) was obtained from the twice-distilled water, which underwent an ion exchange procedure followed by microfiltration (Simplicity UV, Merck Millipore SAS, Darmstadt, Germany). The water sample was analyzed using the ISP-MS technique for 25 elements, 8 of which are presented in Table 1, while the rest had maintenance on the level of $10^{-7}\%$. The total solid residue was below 0.0005%. Therefore, deionized water fits the quality of an ultra-pure reagent. Further, it was also used for the preparation of the KCl and ADMP-F solutions.

A solid sample of high purity KCl (99.0–100.5%; CAS 7447-40-7; Sigma-Aldrich, Burlington, MA, USA) was used to prepare 0.1 mol/L solution with a pH 5.15 in in-house deionized water.

The fluorescent-tagged antiscalant (2-(6-morpholino-1,3-dioxo-1H-benzo[de]isoquinolin-2(3H)yl)ethylazanediyl)bis(methylenephosphonic acid) (ADMP-F, Figure 1) was synthesized according to the literature [25]. ADMP-F was dissolved in in-house deionized water to give 5 mg/mL aqueous solution (pH 4.95) and was kept in a quartz beaker before use. A dosage of 5 mg/L was used to assess (i) the contribution of nanoimpurities introduced by the antiscalant itself, and (ii) the interaction of the antiscalant with natural nanoimpurities present in the basic solvent (water) or in a model KCl aqueous solution. It is important to note that while the specific effects may vary with different antiscalants at the same dosage, the underlying mechanism remains consistent.

2.2. Instruments

Three different counters were used to achieve the purpose of this study (Table 2). A particle counter, SLS-1100 (Particle Measuring Systems Inc., Boulder, CO, USA), was used for particles larger than 100 nm [21]. At the same time, the numerical concentration of nanoparticles larger than 20 nm was measured using the NP counter characterization system NP VISION LLC, Moscow, Russia. Particle concentration measurements are based on ultramicroscopy using a 100 mW laser working at $\lambda = 650$ nm. Videos were recorded via a CMOS camera operating at 50 frames per second (fps) and evaluated via the NP Vision Software. The particles were observed in a focused laser beam in a sample volume about 400 μm long, 30 μm wide, and 10 μm deep. Concentration measurements were taken at each frame of the recorded video and then averaged.

Table 2. Characteristics of particle counters used in this present study.

Particle Counter	Manufacturer	Measuring Principle	Characteristics
SLS-1100	Particle Measuring Systems Inc., Boulder, CO, USA.	Laser light scattering counts in the flow of liquid through the capillary tube.	Size * range: from 100 nm to over 500 nm; channels: 100, 200, 300, 500 nm; maximum concentration: 15,000 particles/mL; zero count: <50 counts; particle concentration measurement error: $\pm 10\%$.
NP Counter	NP VISION LLC, Moscow, Russia.	Nanoparticle counter via ultramicroscopy.	Nanoparticles size range: >20 nm.
Homemade "light sheet" ultramicroscope (LSUM device)	Institute of Spectroscopy of the Russian Academy of Sciences, Moscow, Troitsk, Russia.	Nanoparticle Tracking Analysis via ultramicroscopy.	Nanoparticles size range: >30 nm; along with elastic scattering ultramicroscopy the device has an option of fluorescence detection at $\lambda > 450$ nm.

* Size is denoted as hydrodynamic diameter.

Measurements of the concentration of analyzed NPs with hydrodynamic diameters larger than 30 nm in the solution and their distributions over the hydrodynamic radius were carried out using a highly sensitive laser ultramicroscope "light sheet" (LSUM) developed at the Institute of Spectroscopy of the Russian Academy of Sciences, Moscow, Troitsk [26]. The microscope enabled the reliable visualization of single NPs, detected via inelastic light scattering in the solutions under laser irradiation at a wavelength of 405 nm with a laser emitter power of up to 50 mW. NPs were observed in a laser beam focused into a "light sheet" less than 5 μm thick and about 30 μm high. The signals were measured using a highly sensitive scientific sCMOS camera (pco.edge 5.5-M) operating at up to 100 frames per second (fps). The sizes of the NPs were estimated by analyzing their Brownian motion trajectories (Nanoparticle Tracking Analysis (NTA)-method) using original software developed by G.Silaev, Troitsk, Russia. Measurements of the NP concentration in solutions were made by counting, and subsequently averaging, the number of individual NP images registered in each frame of the recorded video. LSUM has also an additional option to measure fluorescence signals of NPs at $\lambda > 450$ nm. Fluorescence signals were observed using an LP450 optical filter.

Various regression methods were used to estimate the number of nanoparticles beyond the detection limits of the described instruments and technics. The use of nonlinear approximation methods was found to be optimal with the following Equation (1):

$$\log N = -a \cdot \ln(S_N) + b \quad (1)$$

where

N denotes the number of nanoparticles in the sample;

S_N indicates the size of the nanoparticles;

a, b denote variational coefficients in equation.

Parameter fitting was carried out using Microsoft Excel LTSC and Origin 2019b software. As a result, the equation of the curve corresponding to the smallest deviation from the experimental data was chosen as the solution. Error levels did not exceed the deviations observed for the experimental data.

3. Results and Discussion

3.1. Solid Nanoimpurities Content Assessment in Deionized Water and Isopropanol

The number N of particles in 1 mL of solvents, measured by different devices, are presented in Table 3. Some typical images, obtained with an LSUM device, are shown in Figure 2a,b. The analyzed nanoparticles are visualized in the plane of the “light sheet” as individual bright spots on a dark noise background. However, it should be noted that these structures/particles are not directly imaged and only act as point scatterers. Thus, the scale bar in Figure 2 indicates the observation area, but not the real particle sizes, although for a set of the same type heterogeneities in accordance with Rayleigh’s law, the scattered light intensity is directly proportional to D^6 , where D corresponds to the particle diameter. Some spots appear larger, some smaller, due to either different positions in the beam or the different chemical nature of a certain particle. At the same time, an observation of spots depends also on the detection limit of the particular device. In our case, the lower limits correspond to $D = 20$ nm (NP Counter), 30 nm (LSUM device), and 100 nm (SLS-1100). Thus, the particles smaller than 30 nm are invisible in Figure 2 images.

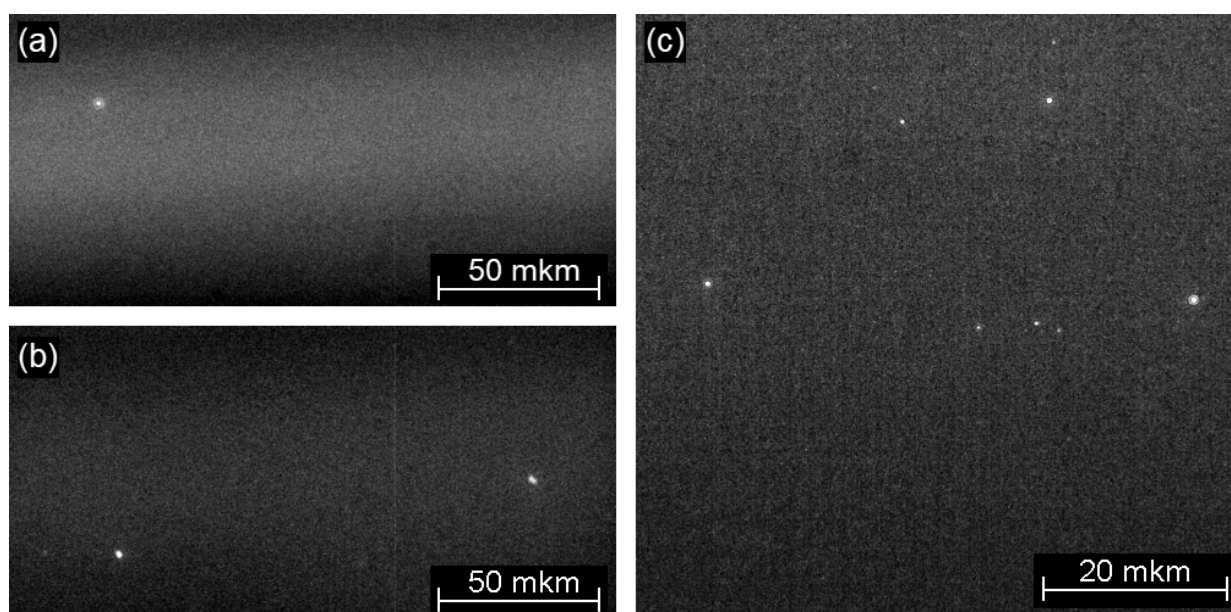


Figure 2. Visualization of single nanoparticles in solvents using light sheet ultramicroscope (LSUM device) via inelastic light scattering at room temperature in isopropanol (a); in deionized water (b); and in 0.1 mol/mL KCl solution in deionized water (c). The scale bar indicates the scale of captured area of images, while the focal depth is approximately 2.5 μm .

It was found that both solvents contained a significant number of particles bigger than 20 nm and these heterogeneities were (i) real objects with macroscopic lifetimes, not fluctuations, and (ii) discrete objects (not bicontinuous phases with large correlation lengths). Indeed, each spot, as registered in Figure 2, had its track. They all entered the field of view of the light beam, remained there, clearly indicating Brownian motion, and then left it. None of them reflected spontaneous density fluctuations of the solvent (water, isopropanol) or of the aqueous solution (KCl; ADMP-F). This result is in good agreement with the observations of Sedlak and Rak [27].

Table 3. Nano/microimpurity concentrations in deionized water and isopropanol.

Fraction Size, nm	Cumulative Particle Concentration, Number N of Particles in 1 mL				Counter
	Deionized Water		Isopropanol		
	N	logN	N	logN	
≥500	23 ± 1	1.4	15 ± 1	1.2	SLS-1100
≥300	48 ± 2	1.7	30 ± 2	1.5	SLS-1100
≥200	141 ± 6	2.2	96 ± 8	2.0	SLS-1100
≥100	1530 ± 13	3.2	782 ± 10	2.9	SLS-1100
≥30	$(4 ± 1) × 10^5$	5.6	<10 ⁴	<4	LSUM device
≥20	$(3 ± 1) × 10^6$	6.5	$(5 ± 3) × 10^5$	5.7	NP Counter
≥1	$(1.2 ± 0.6) × 10^{11}$	11.1	$(8 ± 4) × 10^8$	8.9	extrapolation

The numbers, $(4 ± 1) × 10^5$ and $(3 ± 1) × 10^6$, of foreign particles in 1 mL for deionized H₂O, obtained with the LSUM device and NP counter, are in reasonable agreement with estimations by Mullin [28]: “Aqueous solutions as normally prepared in the laboratory may contain >10⁶ solid particles per cm³ of sizes <1-μm”. Bearing in mind the detection limits, the particle size distribution diagram is also in good agreement with the SLS 1100 measurement results (Figure 3a). Ultra-pure isopropanol demonstrates c.a. one order of magnitude fewer nanoimpurity concentrations relative to deionized water (Table 2). This is also in qualitative agreement with the relative content of chemical elements (Si, Fe, Ca, P, S, etc.) in water and isopropanol, Table 1.

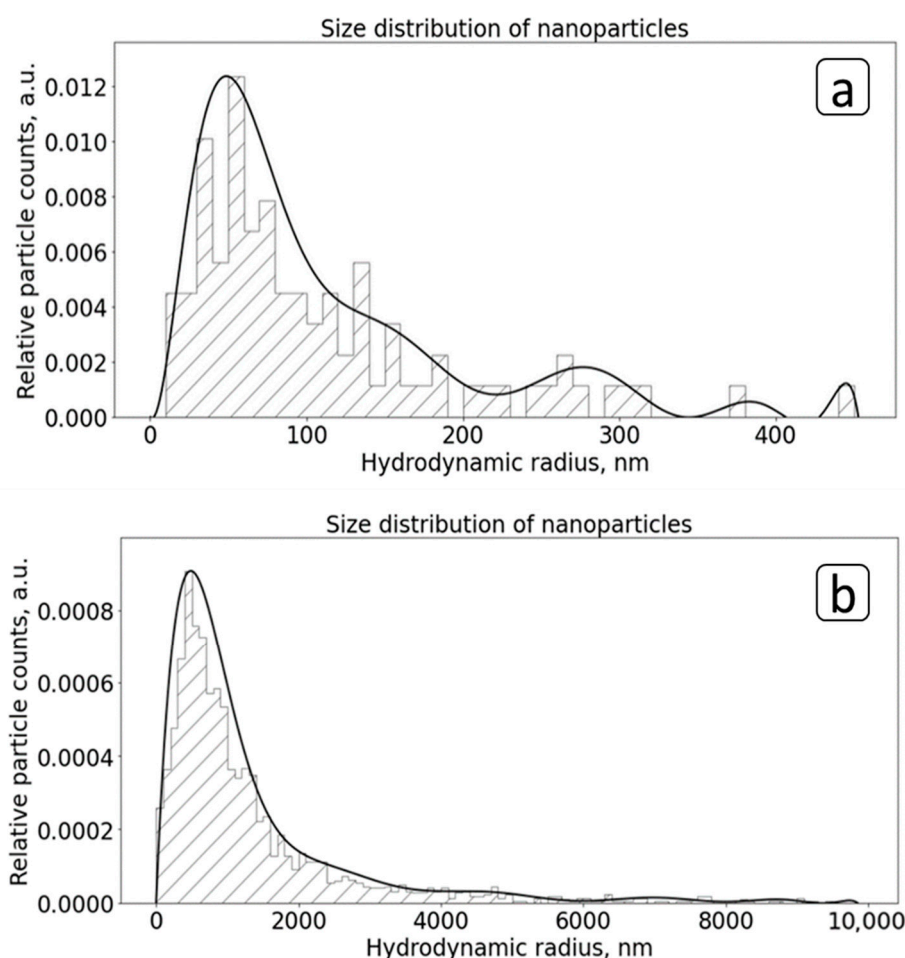


Figure 3. Number-weighted size distributions of foreign nanoparticles in deionized water (a) and in 0.1 mol/mL KCl aqueous solution (b); room temperature, LSUM device.

A sequential build-up of cumulative particles, number N , in 1 mL for fractions with sizes ≥ 500 , ≥ 300 , ≥ 200 , ≥ 100 , ≥ 30 , and ≥ 20 nm provides a unique possibility to make an extrapolation of solid impurity concentrations to a direct undetectable range ≥ 1 nm (Figure 4). This gives rather reasonable values of $(1.2 \pm 0.6) \times 10^{11}$ particles per mL for water and $(8 \pm 4) \times 10^8$ particles per mL for isopropanol.

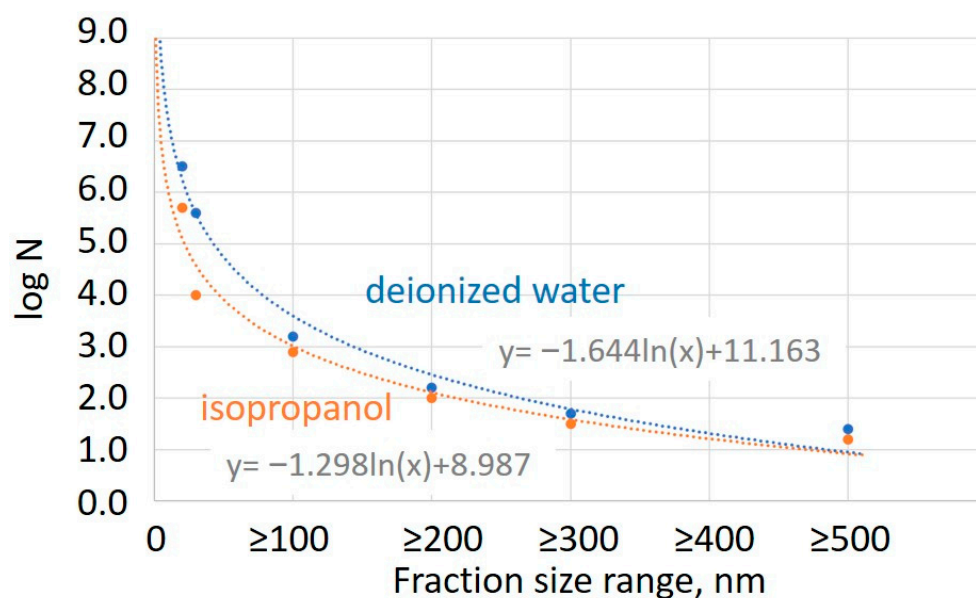


Figure 4. Correlation of particle size and cumulative particle concentration $\log N$, where N denotes the total number of particles in 1 mL exceeding the specified size.

This estimate is based on the assumption that the size distribution trend of nano/microimpurities observed in the 20 to 500 nm range is also applicable to the 1 to 20 nm fraction, which is hypothetically present in the samples. Indeed, the fact that the number of impurities with a size over 100 nm constitutes only 0.1% of those in the range from 20 to 100 nm makes such an assumption reasonable. This enables us to estimate the lower limit of solid concentrations in any aqueous solution prepared on the basis of deionized water. Such an assumption is supported by our previous studies on 0.1 mol/mL CaCl_2 and Na_2SO_4 aqueous solutions, where the fractions of solid impurities with particle sizes ranging from 0.9 to 5 nm have been detected by DLS, and are found to dominate in the particle distribution mode by number [14]. The same fraction was also registered using the DLS technique in electronic grade purity nitric acid [9].

However, even a directly measured value of 3×10^6 particles/mL in deionized water for impurities larger than 20 nm should offer researchers heterogeneous alternatives to the concept of homogeneous reaction pathways in aqueous solutions [29–31]. Regardless, it is virtually impossible to obtain a solvent completely free of foreign matter unless reverse osmosis is used. Careful ultrafiltration can hardly reduce the number of solid nanoimpurities in the aqueous phase to $<10^5$ units per mL, although such an operation may make the solution more or less immune to bulk heterogeneous nucleation.

Thus, we demonstrated that the content of foreign solid nanoparticles is high even in solvents of reagent purity class, not to mention municipal water and feed waters of desalination plants. Consequently, any single molecule of reactant in such a solvent is likely to be near a solid surface in the bulk liquid, with distances in water ranging from 0 to 1000 nm. Therefore, these nanoimpurities should be considered as possible natural precursors of crystallization for any mineral scale. Our results aim to clarify the misconception that working with reagent purity substances excludes bulk heterogeneous nucleation, and to provide some evidence that scale formation can occur not exclusively through the spontaneous homogeneous nucleation mechanism

3.2. Solid Nanoimpurities Content Assessment in Aqueous Solutions of KCl and ADMP-F

The dissolution of KCl in deionized water increases the concentration of foreign particles in water from 3.7×10^5 to 3.1×10^7 particles (larger than 30 nm) per 1 mL (Figure 2c, Table 4). Indeed, a comparison of Figure 2b,c and Figure 3a,b demonstrates that the dissolution of any reagent-grade purity solid salt in deionized water leads, inevitably, to a significant increase in solid impurity concentration. In the particular case of KCl, the relative content of particles with size >100 nm becomes higher, as shown in Figure 3b.

Table 4. Nano/microimpurity concentrations in KCl and ADMP-F solutions in deionized water according to ultramicroscopy, performed with an LSUM device.

Sample	Particle's Detection Mode	Cumulative Particle Concentration, Number N of Particles in 1 mL
Deionized water	Light scattering	$(3.7 \pm 1.9) \times 10^5$
5 mg/mL ADMP-F in deionized water	Light scattering	$(1.6 \pm 0.1) \times 10^8$
	Fluorescence	$(2 \pm 1.5) \times 10^5$
0.1 mol/mL KCl in deionized water	Light scattering	$(3.1 \pm 0.3) \times 10^7$
0.05 mol/mL KCl and 2.5 mg/mL ADMP-F in deionized water	Light scattering	$(6.2 \pm 2.9) \times 10^7$
	Fluorescence	$(1.3 \pm 1.0) \times 10^6$

It is noteworthy that the conventional laboratory procedure of filtering the solution using 200 nm membranes to “remove dust” leaves most of the solid nanoparticles listed in Table 4 in the aqueous phase as potential crystal nucleation centers when the solution is supersaturated.

The most striking results were obtained using fluorescent-labeled antiscalant ADMP-F solution (Figure 5, Table 4). It was found that the dissolution of 5 mg ADMP-F in 1 L of deionized water increases solid impurity content a thousand times, up to 1.6×10^8 units in 1 mL. The usual light scattering mode (Figure 5a) reveals numerous impurities. However, the image drastically changes in the fluorescent light scattering mode (Figure 5b). First of all, the background becomes uniformly light due to individual molecules of the fluorophore. At the same time, some bright spots, indicated by black arrows, are also registered. These were assigned to the solid impurities that have adsorbed ADMP-F.

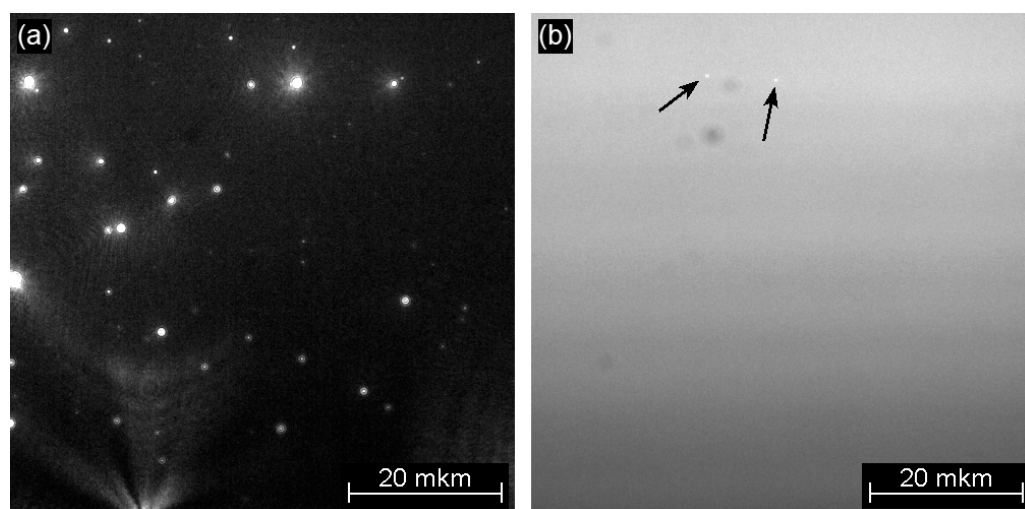


Figure 5. Images of single nanoparticles in ADMP-F solution in deionized water (5 mg/mL), obtained with a light sheet ultramicroscope by inelastic light scattering detection (a) and by detection of fluorescence emission at $\lambda > 450$ nm (b) at room temperature (LSUM device). The arrows denote solid particles that have adsorbed ADMP-F. The scale bar indicates the scale of the captured area of the images, while the focal depth was approximately 2.5 μ m.

Although some of the small faintly glowing particles present in Figure 5a may be lost in the light background of Figure 5b, the number of ADMP-F-bearing solids is smaller than the total content of particle impurities. The LSUM device gives only $N = 2 \times 10^5$ units in 1 mL, although this value is underestimated (Table 4). Thus, the antiscalant covers the surface of only a small part of all particles larger than 30 nm present in the aqueous phase.

The most interesting data have been obtained for the 1:1 volume mixture of 0.1 mol/mL KCl and 5 mg/mL ADMP-F solution in deionized water (Figure 6, Table 4). The usual light scattering mode reveals 6.2×10^7 units in 1 mL (Figure 6a). At the same time, the fluorescent light scattering mode gives 1.3×10^6 ADMP-F bearing particles in 1 mL. This is almost an order of magnitude more than in the ADMP-F initial solution (2×10^5). The result indicates that ADMP-F is selectively adsorbed by some natural solid impurities, present in a true solution of any inorganic salt, but some types of particles do not interact with ADMP-F at all. To the best of our knowledge, this is the first report on natural “nanodust” particle differentiation worldwide. Thus, an important clarification should be made to previous publications on bulk heterogeneous crystallization [14,25,28]: not all types of nanoparticles present in the liquid phase are equally suitable for crystal nucleation and scale inhibition. Generally, it would suffice to selectively remove or mask, via preliminary sorption of antiscalants, only those solid substances that most efficiently initiate crystallization. The challenge lies in identifying which specific substances are targeted by the scale inhibitor. We hypothesize that iron hydroxo/oxides and aluminum hydroxo/oxides significantly contribute to the nucleation rate. However, substantial work is still required to substantiate this hypothesis.

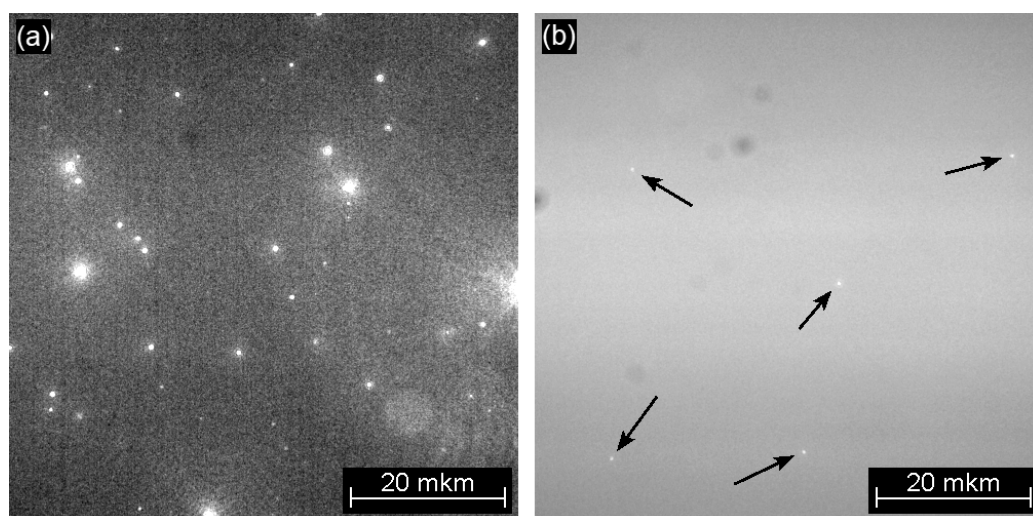


Figure 6. Images of single nanoparticles in a mixed ADMP-F (2.5 mg/mL) and KCl (0.05 mol/mL) solution in deionized water (0.05 mol/mL) obtained via a light sheet ultramicroscope (LSUM device) by recording inelastic light scattering (a) and fluorescence emission at $\lambda > 450$ nm (b) at room temperature. The arrows point to solid particles that have been adsorbed by ADMP-F. The scale bar indicates the scale of the captured image area at a depth of focus of about 2.5 μm .

3.3. Tentative Concentration, Nature, and Role of Natural Solid Nanoimpurities in Aqueous and Nonaqueous Solutions

An extrapolation of the cumulative number of solid impurities to the range over 1 nm gives the lowest level estimates of numerical values of their total content in 1 mL as $N = 10^{11}$ for deionized water and c.a. 10^9 for extra pure isopropanol, respectively (Table 3). In the approximation, where all particle sizes are considered to be 1 nm, it turns out that any single molecule dissolved in such deionized water is close to the solid surface, with a maximum distance of about 1300 nm. The dissolution of any pure substance in these solvents greatly increases the particulate matter content and shortens the maximal distance. Our previous assessment of particulate matter units in 0.09 mol/mL CaCl_2 using different techniques

led to 10^{15} particles in 1 mL with a size of c.a. 1 nm [32]. Recent data for 0.1 mol/mL KCl solution (3×10^7 particles in 1 mL with size >30 nm, Table 4) are in qualitative agreement with those published in [9], bearing in mind the higher purity of KCl relative to CaCl_2 and a different detection range. Thus, any molecules or ions prone to chemical interaction with each other in the bulk aqueous solution occur inevitably within “walking distance” with solid surfaces of impurities that may accelerate or slow down this reaction.

The solid impurities in deionized water are surely very diverse in chemical and phase composition. This follows from the fluorescence data (Figures 5 and 6). ADMP-F molecules are selectively sorbed by only about 10% of the solid units present in the mixed solution of ADMP-F and KCl. Among the chemical elements present in the water, the most suitable candidate is iron (Table 1). Indeed, despite the small content (0.0004 ppm), this element is capable of forming insoluble species $\text{Fe}(\text{OH})_3^{\text{solid}}$ at $5.2 < \text{pH} < 11$ (Figure 7). This chemical characterization diagram was obtained from iron hydrolysis constants taken from the IUPAC Stability Constants Database [33] operating SPECIES Software (Academic Software, Timble, UK) [34] for 25°C and ionic strength $I = 0$ mol/mL. Equilibrium constants for Fe^{3+} , FeOH^{2+} , $\text{Fe}(\text{OH})_2^+$, $\text{Fe}(\text{OH})_4^-$, water soluble $\text{Fe}(\text{OH})_3^{\text{liquid}}$, and solid $\text{Fe}(\text{OH})_3^{\text{solid}}$ species were used. The latter may correspond to different forms of iron hydroxo/oxides, e.g., amorphous $\text{FeO}(\text{OH})$, hematite Fe_2O_3 , and magnetite Fe_3O_4 . Some diversity of constants, presented in [33] by different research groups, makes precise modeling complicated. Nevertheless, at pH 5.8 from 12% to 78% of total iron (0.0004 mg/mL) exists in the solid form. Thus, even traces of iron in deionized water are able to provide the presence of colloidal particles. Notably, this kind of solid impurity is very pH-sensitive: below pH 5, almost all natural iron is represented exclusively by water-soluble species (true solution), while at pH 7, most of it exists in a solid form. Any fluctuations in total iron content make these boundaries flexible. Another type of solid impurity should include silica and silicates of different dispersity (quartz, kaolinite, montmorillonite, illite, etc.), as shown in Table 1. In addition, the presence of colloidal MnO_2 and fine carbon particles cannot be excluded. At the same time, chemical speciations analyses do not reveal the presence of CaCO_3 , gypsum, or $\text{CaHPO}_4 \cdot 2\text{H}_2\text{O}$ solid species in the procedures for the detection of calcium, phosphorus, and sulfur in deionized water (Table 1).

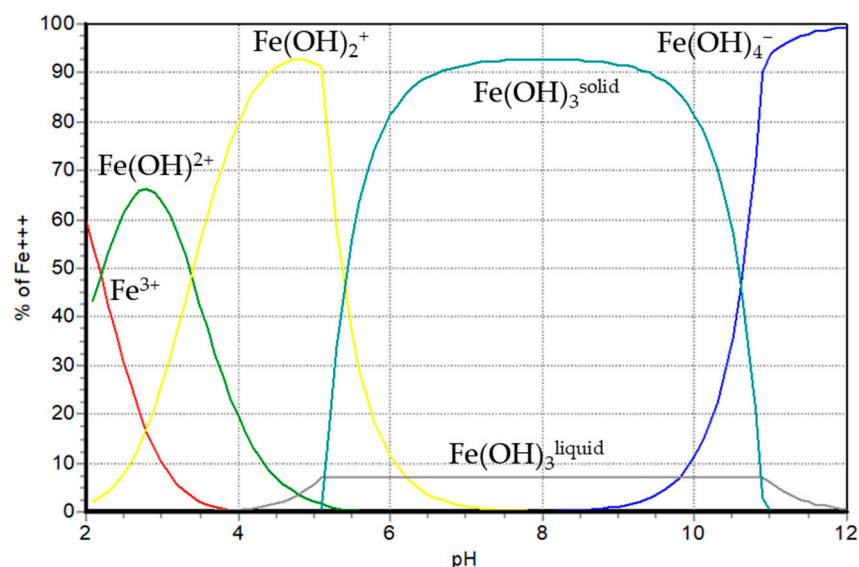


Figure 7. Mole fractions (mole %) of iron(III) in deionized water as a function of pH at 25°C and zero ionic strength for $[\text{Fe}^{3+}] = 7 \times 10^{-6}$ mmol/mL (0.0004 mg/mL); SPECIES software (Academic Software, Timble, UK) [34].

Therefore, even pure deionized water for routine laboratory use usually has a significant content of solid nanoparticles of different natures at the level of 10^{10} – 10^{11} particles

per 1 mL. This is illustrated in Figure 8a, which comprises some refinement of the scheme proposed by M. Sedlák [35]. Figure 8a illustrates a set of potential solid impurities found in deionized water, based on the data presented in Table 1. The figure aims to represent at least three different types of solids: hydroxo/oxides (red color), the silica-based solids (swamp color), and some other solids (blue color).

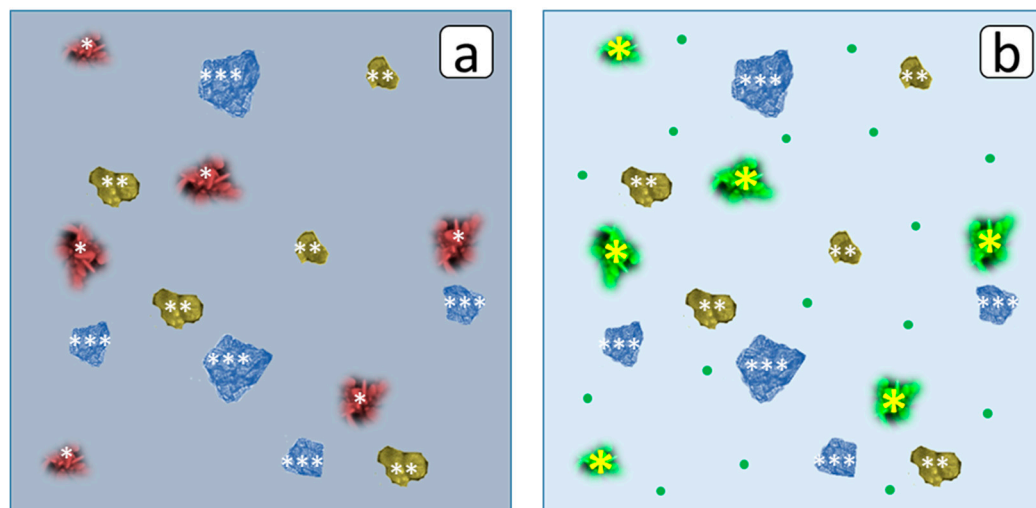


Figure 8. Schematic illustration of possible solid nanoimpurities in deionized water in the absence (a) and in the presence (b) of ADMP-F. The red particles (marked with *) denote iron hydroxo/oxides, the swamp-colored particles denote silica-based solids (marked with **); the blue (marked with ***) are other solids; and the green particles (marked with yellow *) are iron hydroxo/oxides covered with ADMP-F layer. Green circles indicate “free” ADMP-F molecules, while solvent molecules are assumed to occupy the rest.

It should be noted that most modern research methods relating to nanoparticle characterization in their liquid phase, such as X-ray Ptychography, Small-Angle X-ray Scattering (SAXS), Transmission Electron Microscopy (TEM), Field Emission Scanning Electron Microscopy (FESEM), etc. [36–38], are not applicable to the solutions with trace quantities of solids, present at the ppb level. The precise identification of the morphology of such impurities remains challenging. Some of these impurities may be amorphous, and any attempt to remove the solvent to isolate them as a solid could result in irreversible changes in morphology or the isolation of chemical forms that do not exist in the liquid state.

Isopropanol reveals two orders of magnitude lower concentrations of nanoimpurities, although it is still high at 8×10^8 . An injection of any reagent-grade chemicals into these solvents leads to multiple increases in the amount of such impurities. At the same time, each of the reagents, added to the solvent, inevitably brings its own set of impurities, which may be partly or totally different from those present in the solvent. This was clearly demonstrated in the present study for KCl and ADMP-F aqueous solutions. Some of these nanoimpurities can potentially participate in seemingly homogeneous chemical reactions.

For example, the crystal nucleation in supersaturated aqueous solutions of inorganic salts is broadly recognized as a heterogeneous process, with solid nanoimpurities acting as nucleation centers [9,11,12,14–16,28]. At the same time, phosphonic acids are known to retard an undesirable scale formation of poorly soluble salts [39–41]. It was recently supposed that the scale inhibition effect is primarily due to the blockage of nanoimpurities by the antiscalant [16,25,32].

Our current data on the location of the fluorescent marker represent a new step in understanding this phenomenon. They demonstrate clearly that only a small part of all nano/microimpurities present in the aqueous phase are blocked by the antiscalant ADMP-F, which is highly effective in inhibiting the formation of CaCO_3 and $\text{CaSO}_4 \cdot 2\text{H}_2\text{O}$ scales [25]. Presumably, the nanoimpurities of iron hydroxo/oxides are blocked by ADMP-F to the

greatest extent, although sorption of this antiscalant by other types of nanoimpurities should not be excluded. This process is shown in Figure 8b as a change of the red color of iron hydroxo/oxides species to green, typical for the fluorescence of ADMP-F. This is in good agreement with the high affinity of phosphonates to iron(III) ions. Another important aspect is that most of the antiscalant molecules remain in solutions in an unadsorbed form (in Figure 8b, ADMP-F molecules are indicated by tiny green dots and a lighter image background compared to 8a). The molecular species of “free” ADMP-F form a depot species ready to block solid impurities in any salt solution, as demonstrated for KCl (Figure 6). Additionally, the excess of molecular antiscalant species helps to explain the previously observed coating of the sediment surface of calcite and gypsum by uniform fluorescent layers of antiscalant after scale formation [25]. Almost all phenomena related to scale crystallization and the inhibition of crystal precipitation can receive a quite consistent explanation on the basis of solid nanoimpurities.

Meanwhile, our data do not exclude the so-called homogeneous pre-nucleation cluster (PNC) pathway [29–31]. PNCs can adsorb sequentially on some types of solid nanoimpurities and provide further deposit formation at this stage. Otherwise, the crucial role of sedentary polyacrylate macromolecules in scale inhibition has no reasonable explanation if a PNC pathway is exclusively considered. In any case, one cannot ignore the presence of a wide set of natural solid impurities, which represent the ready crystal nucleation centers in “walking distance” in the bulk supersaturated aqueous solution of any poorly soluble salt. We hope that our present results will provide some arguments to the long-term discussion on whether heterogeneous nucleation or homogeneous nucleation mechanisms control the scale formation process [14,16,28–31,42–47]. This result is also in good agreement with the ideas expressed in [41]. It is reasonable to assume that one kind of nanoimpurity would provide embryos of sparingly soluble salt with one set of crystal fast-growing faces, while another kind of nanosolid would initiate the less active formation of crystals nuclei and promote the preferential growth of different faces of the same crystal. Thus, the blockage of the first kind of impurity by antiscalant may result both in the reduction of crystal growth rate and a corresponding change in crystal habit

Indirect confirmation of the present results was obtained by us in recent experiments with wood shavings [48]. The cellulose material selectively sorbed iron and alumina hydroxo/oxides, but did not affect other impurities. However, this was sufficient to increase the efficacy of the antiscalant against gypsum scale formation.

At the same time, our data are far from being limited to the field of crystallization and scale inhibition. They give independent support to the ideas, expressed by Sedlak [17,19,27,35] and Kononov [18], on the roles of loose and tight domains for organic reactions in a liquid medium. Indeed, different types of natural nano/microimpurities in aqueous and nonaqueous solutions may serve as heterogeneous, well-dissipated catalytic species for a broad spectrum of chemical reactions that have been, so far, wrongly considered as homogeneous processes.

Our findings suggest a shift in focus for current scale inhibition research, moving away from studying antiscalant and scale interactions towards exploring antiscalant interactions with nanoparticles. To date, some water treatment researchers have speculated that scale nucleation occurs spontaneously in their laboratory samples via a homogeneous mechanism [29–31,44–47]. Meanwhile, we demonstrate here that the bulk heterogeneous mechanism is much more likely to take place; even as far as in pure solvents, there is c.a. over 1,000,000 potential crystallization centers in 1 mL, to say nothing of tap or feed water. At the same time, we have experimentally demonstrated for the first time that antiscalant blocks only a few percents of this amount, presumably iron hydroxo/iron oxides. It is an important step forward relative to previous reports on bulk heterogeneous crystallization [14,25,28,32]. Thus, it is more reasonable to look for compounds that block iron or aluminum hydroxo/oxides rather than the surface of gypsum or calcite.

Therefore, we firmly believe that significant progress in understanding chemical reactivity can only be made by expanding and deepening our knowledge of the nature, concentration, and size of natural nano- and microimpurities in liquid reagents.

4. Conclusions

Using direct particle counting via laser ultramicroscopy, it was found that even high-purity laboratory solvents, such as deionized water and isopropanol, contain solid nanoparticles larger than 20 nm, with concentrations of 10^6 and 10^5 units/mL, respectively. It was further demonstrated that extrapolating these values to particle sizes larger than 1 nm results in total impurity concentrations as high as 10^{11} units/mL for water and 10^8 units/mL for isopropanol. Increasing the concentration of the reagent significantly reduces the distance between the particles. Therefore, the possibility of reagent interactions in the seemingly homogeneous liquid phase via a heterogeneous mechanism should not be excluded or disregarded.

It was demonstrated that any reagent-grade purity chemical, added to deionized water, brings its own set of solid matter nanocontaminants not necessarily matching the composition of solids present in water.

It has been experimentally confirmed that nanocontaminants represent a mixture of particles with different chemical natures. One type of impurity tends to adsorb ADMP-F, while others show very low affinity for this antiscalant, if at all, and leave most of the ADMP-F molecules “free”. Thus, the fluorescent-tagged aminobisphosphonates are capable of differentiating the particulate matter traces present in the reagent-grade purity solutions.

ICP-MS, laser ultramicroscopy, and chemical speciation data comparisons allow us to identify some solid contaminants in water and in KCl aqueous solutions as silica-based species and iron(III) hydroxo/oxides. The latter belongs to the least representative fraction. However, this exact type of nanocontaminants is likely to be responsible for the bulk heterogeneous nucleation of calcite, gypsum, and other salts in the supersaturated aqueous solutions. Thus, this study provides further support for scale inhibition mechanisms, suggesting that antiscalants block nanoimpurities that serve as crystal nucleation centers. Moreover, it offers a significant refinement, suggesting that not all nanoimpurities are blocked, but rather specific types, presumably the most active ones, are targeted.

The role of nanoimpurities must be seriously taken into account, especially in the case of scale inhibition applications. However, a comprehensive examination of the role of natural nanoimpurities in chemical processes could undoubtedly open new horizons and dispel misconceptions across various fields of chemistry and chemical technology.

Author Contributions: Conceptualization, K.P. and M.B.; methodology, K.P., G.S. and Y.V.; validation, K.P., E.K., M.O., V.K., M.T. and M.B.; formal analysis, K.P., E.K. and M.O.; investigation, G.S., E.K., V.K., M.T. and M.B.; writing—original draft preparation, K.P.; supervision, Y.V. and V.T.; project administration, V.T.; resources, V.T.; visualization, G.S. and A.O.; writing—review and editing, M.O., Y.V., V.T. and A.O. All authors have read and agreed to the published version of the manuscript.

Funding: This research received no external funding.

Data Availability Statement: The data presented in this study are available on request from the corresponding author.

Conflicts of Interest: The authors declare no conflicts of interest.

References

1. Nowack, B.; Bucheli, T.D. Occurrence, behavior and effects of nanoparticles in the environment. *Environ. Pollut.* **2007**, *150*, 5–22. [[CrossRef](#)] [[PubMed](#)]
2. Bundschuh, M.; Filser, J.; Lüderwald, S.; McKee, M.S.; Metreveli, G.; Schaumann, G.E.; Schulz, R.; Wagner, S. Nanoparticles in the Environment: Where Do We Come From, Where Do We Go To? *Environ. Sci. Eur.* **2018**, *30*, 6. [[CrossRef](#)] [[PubMed](#)]
3. Mustamam, M.K.; Elaissari, A.; Fatehah, M.O.; Aziz, H.A.; Wang, M.H.S. Nano Pollutant Properties, Occurrence and Behavior in Water and Wastewater Streams. In *Industrial Waste Engineering*; Springer: New York, NY, USA, 2024; pp. 279–332. [[CrossRef](#)]

4. Chen, Y.; Bergendahl, J. Identification and Quantification of a Wide Variety of Inorganic Nanoparticles in Municipal Wastewater. *J. Hazard. Toxic Radioact. Waste* **2021**, *25*, 04021030. [[CrossRef](#)]
5. Singh, S.; Prasad, S.M.; Bashri, G. Fate and toxicity of nanoparticles in aquatic systems. *Acta Geochim.* **2022**, *42*, 63–76. [[CrossRef](#)]
6. Jabbar, K.Q.; Barzinjy, A.A.; Hamad, S.M. Iron oxide nanoparticles: Preparation methods, functions, adsorption and coagulation/flocculation in wastewater treatment. *Environ. Nanotechnol. Monit. Manag.* **2022**, *17*, 100661. [[CrossRef](#)]
7. Wigginton, N.S.; Haus, K.L.; Hochella, M.F., Jr. Aquatic environmental nanoparticles. *J. Environ. Monit.* **2007**, *9*, 1306–1316. [[CrossRef](#)] [[PubMed](#)]
8. Lead, J.R.; Wilkinson, K.J. Aquatic Colloids and Nanoparticles: Current Knowledge and Future Trends. *Environ. Chem.* **2006**, *3*, 159–171. [[CrossRef](#)]
9. Popov, K.; Oshchepkov, M.; Kovalenko, A.; Redchuk, A.; Dikareva, J.; Pochitalkina, I. Scale nucleation natural precursors: A case study of “micro/nanodust” impurities nature in laboratory aqueous samples obtained from Moscow tap water. *Int. J. Corros. Scale Inhib.* **2020**, *9*, 1097–1112. [[CrossRef](#)]
10. Becker, H.; Murawski, J.; Shinde, D.V.; Stephens, I.E.L.; Hinds, G.; Smith, G. Impact of impurities on water electrolysis: A review. *Sustain. Energy Fuels* **2023**, *7*, 1565–1603. [[CrossRef](#)]
11. Briard, M.; Brandel, C.; Dupray, V. Strong Enhancement of Nucleation Efficiency of Aqueous Ethylenediamine Sulfate Solutions by Nonphotochemical Laser-Induced Nucleation: Investigations on the Role of Solid Impurities in the Mechanism. *Cryst. Growth Des.* **2023**, *23*, 7169–7178. [[CrossRef](#)]
12. Cao, T.; Rolf, J.; Wang, Z.; Violet, C.; Elimelech, M. Distinct impacts of natural organic matter and colloidal particles on gypsum crystallization. *Water Res.* **2022**, *218*, 118500. [[CrossRef](#)] [[PubMed](#)]
13. Tyumentsev, V.A.; Fazlitdinova, A.G.; Dozhdikova, D.V.; Krivtsov, I.V. Effect of nanoadditives on the kinetics of $\text{CaSO}_4 \cdot 2\text{H}_2\text{O}$ formation and the mosaic structure of crystals. *Inorg. Mater.* **2014**, *51*, 68–70. [[CrossRef](#)]
14. Oshchepkov, M.; Popov, K.; Kovalenko, A.; Redchuk, A.; Dikareva, J.; Pochitalkina, I. Initial Stages of Gypsum Nucleation: The Role of “Nano/Microdust”. *Minerals* **2020**, *10*, 1083. [[CrossRef](#)]
15. Wang, L.-T.; Ge, H.-H.; Han, Y.-T.; Wan, C.; Sha, J.-Y.; Sheng, K. Effects of Al_2O_3 nanoparticles on the formation of inorganic scale on heat exchange surface with and without scale inhibitor. *Appl. Therm. Eng.* **2019**, *151*, 1–10. [[CrossRef](#)]
16. Trukhina, M.; Popov, K.; Tkachenko, S.; Vorob’Eva, A.; Rudakova, G. Impact of colloidal iron hydroxide and colloidal silicon dioxide on calcium sulfate crystallization in the presence of antiscalants. *Int. J. Corros. Scale Inhib.* **2022**, *11*, 1147–1171. [[CrossRef](#)]
17. Rak, D.; Sedlák, M. Solvophobicity-Driven Mesoscale Structures: Stabilizer-Free Nanodispersions. *Langmuir* **2023**, *39*, 1515–1528. [[CrossRef](#)] [[PubMed](#)]
18. Kononov, L.O.; Fukase, K.; Bunkin, N.F. Editorial: Chemical reactivity and solution structure. *Front. Chem.* **2023**, *11*, 1293697. [[CrossRef](#)] [[PubMed](#)]
19. Sedlák, M.; Rak, D. On the Origin of Mesoscale Structures in Aqueous Solutions of Tertiary Butyl Alcohol: The Mystery Resolved. *J. Phys. Chem. B* **2014**, *118*, 2726–2737. [[CrossRef](#)] [[PubMed](#)]
20. *D 5127*; Standard Guide for Ultra-Pure Water Used in the Electronics and Semiconductor Industries. ASTM International: Conshohocken, PA, USA, 2018.
21. Ultra DI[®] 20 Plus Liquid Optical Particle Counter, Particle Measuring Systems. Available online: <https://archive.pmeasuring.com> (accessed on 20 March 2024).
22. NanoSight NS 300, Malvern Panalytical. Available online: <https://kdsi.ru/oborudovanie/nanosight/nanosight-ns300/> (accessed on 20 March 2024).
23. Filipe, V.; Hawe, A.; Jiskoot, W. Critical Evaluation of Nanoparticle Tracking Analysis (NTA) by NanoSight for the Measurement of Nanoparticles and Protein Aggregates. *Pharm. Res.* **2010**, *27*, 796–810. [[CrossRef](#)] [[PubMed](#)]
24. Hole, P.; Sillence, K.; Hannell, C.; Maguire, C.M.; Roesslein, M.; Suarez, G.; Capracotta, S.; Magdolenova, Z.; Horev-Azaria, L.; Dybowska, A.; et al. Interlaboratory comparison of size measurements on nanoparticles using nanoparticle tracking analysis (NTA). *J. Nanoparticle Res.* **2013**, *15*, 2101. [[CrossRef](#)] [[PubMed](#)]
25. Tkachenko, S.; Trukhina, M.; Ryabova, A.; Oshchepkov, M.; Kamagurov, S.; Popov, K. Fluorescent-Tagged Antiscalants—The New Materials for Scale Inhibition Mechanism Studies, Antiscalant Traceability and Antiscalant Efficacy Optimization during CaCO_3 and $\text{CaSO}_4 \cdot 2\text{H}_2\text{O}$ Scale Formation. *Int. J. Mol. Sci.* **2023**, *24*, 3087. [[CrossRef](#)] [[PubMed](#)]
26. Silaev, G.O.; Krashennnikov, V.N.; Shaidulin, A.T.; Uvarov, O.V.; Orlovskaya, E.O.; Orlovskii, Y.V.; Vainer, Y.G. Optical and Electron Microscopy of Clusters of $\text{Nd}^{3+}:\text{LaF}_3$ Nanoparticles Synthesized by the HTMW Method. *Phys. Wave Phenom.* **2023**, *31*, 160–170. [[CrossRef](#)]
27. Sedlák, M.; Rak, D. Large-Scale Inhomogeneities in Solutions of Low Molar Mass Compounds and Mixtures of Liquids: Supramolecular Structures or Nanobubbles? *J. Phys. Chem. B* **2013**, *117*, 2495–2504. [[CrossRef](#)] [[PubMed](#)]
28. Mullin, J.W. *Crystallization*, 4th ed.; Butterworth-Heinemann, Reed Educational and Professional Publishing Ltd.: Oxford, MA, USA, 2001; p. 192.
29. Gebauer, D. How Can Additives Control the Early Stages of Mineralisation? *Minerals* **2018**, *8*, 179. [[CrossRef](#)]
30. Duchstein, P.; Schodder, P.I.; Leupold, S.; Dao, T.Q.N.; Kababya, S.; Cicconi, M.R.; de Ligny, D.; Pipich, V.; Eike, D.; Schmidt, A.; et al. Small-Molecular-Weight Additives Modulate Calcification by Interacting with Prenucleation Clusters on the Molecular Level **. *Angew. Chem. Int. Ed.* **2022**, *61*, e202208475. [[CrossRef](#)] [[PubMed](#)]

31. Xu, S.; Cao, D.; Liu, Y.; Wang, Y. Role of Additives in Crystal Nucleation from Solutions: A Review. *Cryst. Growth Des.* **2021**, *22*, 2001–2022. [[CrossRef](#)]
32. Trukhina, M.; Tkachenko, S.; Ryabova, A.; Oshchepkov, M.; Redchuk, A.; Popov, K. Calcium Sulfate Crystallization in Presence of Fluorecent-Tagged Polyacrylate and Some Refinement of Scale Inhibition Mechanism. *Minerals* **2023**, *13*, 559. [[CrossRef](#)]
33. *Stability Constants Database and Mini-SCDatabase, IUPAC, Version 5.3*; Academic Software: Timble, UK, 2011.
34. Powell, K.J. *Species, in "Solution Equilibria: Principles and Applications (for Windows 95, 98 and NT)", Release 1*; Academic Software: Timble, UK, 1999.
35. Sedláč, M. Large-Scale Supramolecular Structure in Solutions of Low Molar Mass Compounds and Mixtures of Liquids: I. Light Scattering Characterization. *J. Phys. Chem. B* **2006**, *110*, 4329–4338. [[CrossRef](#)] [[PubMed](#)]
36. Calcaterra, H.A.; Zheng, C.Y.; Seifert, S.; Yao, Y.; Jiang, Y.; Mirkin, C.A.; Deng, J.; Lee, B. Hints of Growth Mechanism Left in Supercrystals. *ACS Nano* **2023**, *17*, 15999–16007. [[CrossRef](#)] [[PubMed](#)]
37. Mendoza-Sánchez, A.R.; Hernández-Rodríguez, Y.; Casas-Espínola, J.; Cigarroa-Mayorga, O. Nanostructural modulation of Schottky barrier in Au/ α -MoO₃ heterojunction via Au nanoparticle size control. *Appl. Surf. Sci.* **2024**, *670*, 160624. [[CrossRef](#)]
38. Li, W.-J.; Shi, E.-W.; Zhong, W.-Z.; Yin, Z.-W. Growth mechanism and growth habit of oxide crystals. *J. Cryst. Growth* **1999**, *203*, 186–196. [[CrossRef](#)]
39. Mady, M.F.; Abdelaal, A.T.; Kelland, M.A.; Liakaki-Stavropoulou, S.; Demadis, K.D. Flexible, Linear, and Systematically Expanded Tetraphosphonate Bolaamphiphiles and Their Inhibition Performance against Calcite and Barite Scale Formation. *Energy Fuels* **2023**, *37*, 9176–9184. [[CrossRef](#)]
40. Mady, M.F.; Abdel-Azeim, S.; Kelland, M.A. Antiscalant Evaluation and Quantum Chemical Studies of Nitrogen-Free Organophosphorus Compounds for Oilfield Scale Management. *Ind. Eng. Chem. Res.* **2021**, *60*, 12175–12188. [[CrossRef](#)]
41. Liu, Y.; Zhang, P. Review of Phosphorus-Based Polymers for Mineral Scale and Corrosion Control in Oilfield. *Polymers* **2022**, *14*, 2673. [[CrossRef](#)]
42. Schroeder, S.L.M. Homogeneous Organic Crystal Nucleation Rates in Solution from the Perspective of Chemical Reaction Kinetics. *Crystals* **2024**, *14*, 349. [[CrossRef](#)]
43. Liu, X.Y. Heterogeneous nucleation or homogeneous nucleation? *J. Chem. Phys.* **2000**, *112*, 9949–9955. [[CrossRef](#)]
44. Zhang, T.H.; Zhang, Z.C.; Cao, J.S.; Liu, X.Y. Can the pathway of stepwise nucleation be predicted and controlled? *Phys. Chem. Chem. Phys.* **2019**, *21*, 7398–7405. [[CrossRef](#)] [[PubMed](#)]
45. Zhang, Y.; Li, B.; Liu, J.; Han, D.; Rohani, S.; Gao, Z.; Gong, J. Inhibition of Crystal Nucleation and Growth: A Review. *Cryst. Growth Des.* **2024**, *24*, 2645–2665. [[CrossRef](#)]
46. Men, H. A molecular dynamics study on the boundary between homogeneous and heterogeneous nucleation. *J. Chem. Phys.* **2024**, *160*, 094702. [[CrossRef](#)] [[PubMed](#)]
47. Jun, Y.-S.; Zhu, Y.; Wang, Y.; Ghim, D.; Wu, X.; Kim, D.; Jung, H. Classical and Nonclassical Nucleation and Growth Mechanisms for Nanoparticle Formation. *Annu. Rev. Phys. Chem.* **2022**, *73*, 453–477. [[CrossRef](#)] [[PubMed](#)]
48. Trukhina, M.; Popov, K.; Oshchepkov, M.; Tkachenko, S.; Vorob'eva, A.; Guseva, O. Enhancement of Polyacrylate Antiscalant Activity during Gypsum Deposit Formation with the Pretreatment of Aqueous Solutions with Spruce Wood Shavings. *Materials* **2023**, *16*, 6516. [[CrossRef](#)]

Disclaimer/Publisher's Note: The statements, opinions and data contained in all publications are solely those of the individual author(s) and contributor(s) and not of MDPI and/or the editor(s). MDPI and/or the editor(s) disclaim responsibility for any injury to people or property resulting from any ideas, methods, instructions or products referred to in the content.